nature physics

SUPPLEMENTARY INFORMATION

DOI: 10.1038/NPHYS4149

In the format provided by the authors and unedited.

Large orbital polarization in a metallic square-planar nickelate

Junjie Zhang,[1,*] A. S. Botana,[1] J. W. Freeland,[2] D. Phelan,[1] Hong Zheng,[1] V. Pardo,[3,4] M. R. Norman,[1] J. F. Mitchell[1]

[1]Materials Science Division, Argonne National Laboratory, Argonne, Illinois 60439, USA

[2]Advanced Photon Source, Argonne National Laboratory, Argonne, Illinois 60439, USA

[3]Departamento de Fisica Aplicada, Universidade de Santiago de Compostela, E-15782 Santiago de Compostela, Spain

[4]Instituto de Investigacions Tecnoloxicas, Universidade de Santiago de Compostela, E-15782 Santiago de Compostela, Spain

*E-mail: junjie@anl.gov or junjie.zhang.sdu@gmail.com

S.1 Laboratory XRD measurements

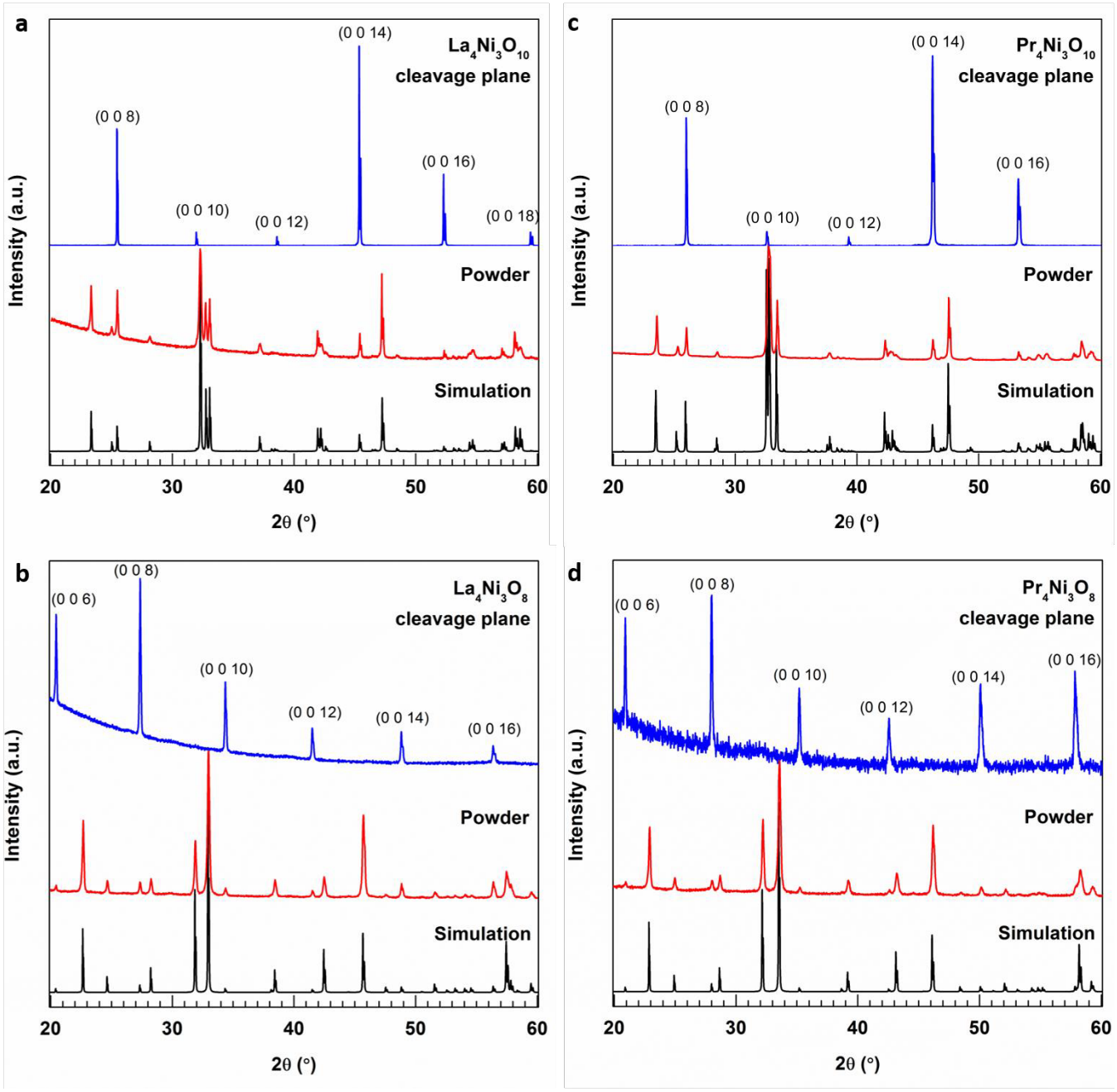

Supplemental Fig. 1. Laboratory XRD measurements of powder and (001) oriented single crystals of $R_4Ni_3O_{10}$ and $R_4Ni_3O_8$ (R=La, Pr). (a) $La_4Ni_3O_{10}$. (b) $La_4Ni_3O_8$. (c) $Pr_4Ni_3O_{10}$. (d) $Pr_4Ni_3O_8$. Both $La_4Ni_3O_{10}$ and $Pr_4Ni_3O_{10}$ are monoclinic. The extracted unit cell parameters are a=5.41 Å, b=5.46 Å, c=27.96 Å and β=90.1° for $La_4Ni_3O_{10}$, and a=5.37 Å, b=5.46 Å, c=27.5 Å and β=90.3° for $Pr_4Ni_3O_{10}$.

S.2 Single crystal x-ray diffraction.

Single crystal X-ray diffraction data of $Pr_4Ni_3O_8$ were collected using a Bruker SMART APEX-II CCD area detector on a D8 goniometer operated with graphite-monochromated Mo Kα radiation (λ = 0.71073 Å). Preliminary lattice parameters and orientation matrices were obtained from three sets of frames. Data integration and cell refinement were done by the INTEGRATE program of the APEX2 software, and multiscan absorption corrections were applied using the SCALE program for area detector[1]. The structure was solved in the *I*4/*mmm* space group by direct methods and refined with full matrix least-squares methods on F^2. All atoms were modeled using anisotropic displacement parameters (ADPs), and the refinements converged for $I > 2\sigma(I)$. Calculations were performed using the SHELXTL crystallographic software package[2]. Details of crystal parameters, data collection, structure refinement and atomic positions are summarized in Supplemental Table 1 and 2. Further details of the crystal structure investigation(s) may be obtained from Fachinformationszentrum Karlsruhe, 76344 Eggenstein-Leopoldshafen, Germany (fax: (+49)7247-808-666; e-mail: crysdata@fiz-karlsruhe.de, https://www.fiz-karlsruhe.de/en/leistungen/kristallographie/kristallstrukturdepot.html), on quoting the deposition number CSD-429797.

Supplemental Table 1. Crystal data and structure refinement of $Pr_4Ni_3O_8$ at room temperature.

Empirical formula	$Pr_4Ni_3O_8$
Formula weight	867.77
Temperature	300(2) K
Wavelength	0.71073 Å
Crystal system, space group	Tetragonal *I*4/*mmm*
Unit cell dimensions	$a = b = 3.93470(10)$ Å $c = 25.4850(9)$ Å
Volume, *Z*	394.56(2) Å^3, 2
Density (calculated)	7.304 g/cm^3
Absorption coefficient	31.210 mm^{-1}
F(000)	768
Crystal size	0.061 × 0.041 × 0.039 mm^3
θ range for data collection	3.197 to 31.278°
Reflections collected/Independent	2584/242 [$R_{int} = 0.0260$]
Completeness to $\theta = 14.357°$	98.6%
Refinement method	Full-matrix least-squares on F^2
Data / restraints / parameters	242 / 0 / 21
Goodness-of-fit	1.065
Final *R* indices [$I > 2\sigma(I)$]	$R_{obs} = 0.0164$, $wR_{obs} = 0.0404$
R indices [all data]	$R_{all} = 0.0232$, $wR_{all} = 0.0435$
Largest diff. peak and hole	1.386 and -1.270 e·Å^{-3}

$R = \Sigma||F_o|-|F_c|| / \Sigma|F_o|$, $wR = \{\Sigma[w(|F_o|^2 - |F_c|^2)^2] / \Sigma[w(|F_o|^4)]\}^{1/2}$ and $w=1/[\sigma^2(Fo^2)+(0.0233P)^2+3.8539P]$ where $P=(Fo^2+2Fc^2)/3$

Supplemental Table 2. Atomic coordinates and equivalent isotropic displacement parameters (Å^2) with estimated standard deviations in parentheses for $Pr_4Ni_3O_8$.

Label	Wyckoff position	*I*4/*mmm*			Occupancy	U_{eq}
		x	*y*	*z*		
Pr(1)	4*e*	0	0	0.4337(1)	1	0.011(1)
Pr(2)	4*e*	0	0	0.2987(1)	1	0.011(1)
Ni(1)	2*a*	0	0	0	1	0.009(1)
Ni(2)	4*e*	0	0	0.1249(1)	1	0.011(1)
O(1)	4*c*	0	0.5	0	1	0.013(2)
O(2)	8*g*	0	0.5	0.1261(2)	1	0.015(1)
O(3)	4*d*	0	0.5	0.2500	1	0.012(1)

U_{eq} is defined as one third of the trace of the orthogonalized U_{ij} tensor.

S.3 X-ray absorption spectroscopy (XAS)

To determine the valence state of $R_4Ni_3O_8$ (R=La, Pr), we measured the shift between the inflection point of the $R_4Ni_3O_{10}$ samples and a Ni^{2+} reference sample. Energy scales were calibrated between samples using a Ni^{2+} measured simultaneously with all the spectra, which allows us to align the spectra within < 0.1 eV. The shift in the inflection point between the $R_4Ni_3O_{10}$ sample and the Ni^{2+} is ~ 0.7 eV, which is consistent with the ~1 eV per 1 e^- charge[3-6] seen between Ni^{3+} and Ni^{2+}. There is an additional shift to lower energy of ~0.7 eV for the $R_4Ni_3O_8$ sample which is consistent with a valence state of $Ni^{1.3+}$ (see Supplemental Fig. 2). The result on $La_4Ni_3O_8$ is also in good agreement with previous hard XAS on powder samples[7].

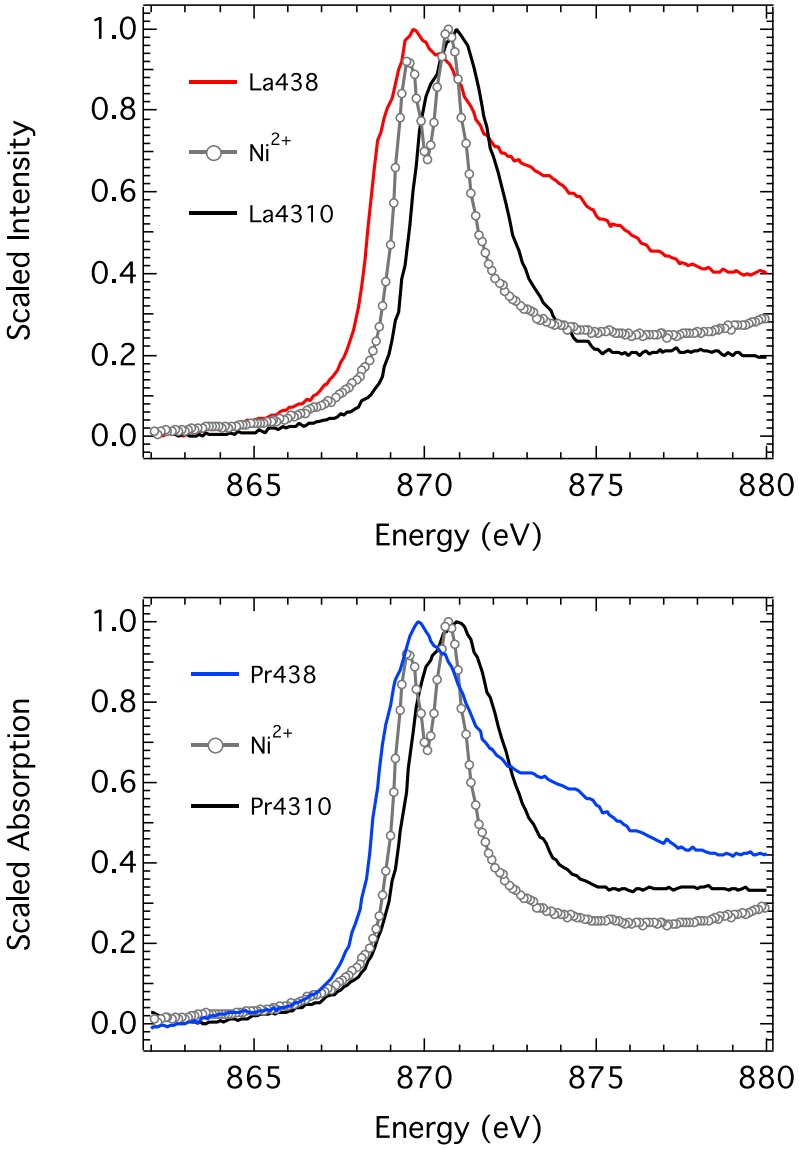

Supplemental Fig. 2. Polarization averaged XAS for $R_4Ni_3O_8$ and $R_4Ni_3O_{10}$ (R=La, Pr) compared to Ni^{2+} (Ref. 8). Pr438: $Pr_4Ni_3O_8$; La438: $La_4Ni_3O_8$. The XAS is averaged via (pol. along *ab* + pol. along *c*)/2. Data have been scaled and background subtracted following the procedures described below.

In Supplemental Fig. 3*a*, we have included an unscaled polarization dependent XAS scan across the L_2 edge to show how we have chosen to normalize the data. For these measurements, the sample angle is at a grazing angle of 15 deg. and the polarization dependence is measured by changing the source polarization without moving the sample. First, we discuss the $Pr_4Ni_3O_8$ data. These data are multiplied by 0.5 since the FY is much stronger for this sample, which is likely due to the strong absorption at the La M edges for the $La_4Ni_3O_8$ compound. To apply the sum rule we focused on the L_2 edge since the self absorption is very strong at the L_3 and therefore the L_2 is more representative of the true XAS. Note also the polarization dependence extends over a wide range between the edges, which is seen in other layered compounds such as cuprates. Since we know the XAS from the empty d-states is limited to at most 5-10 eV above the edge, we chose to focus on that region and exclude the extended edge. To do this for the case of $Pr_4Ni_3O_8$, we simply subtracted a constant value until the position of the pre-edge and post-edge match with only a tiny multiplicative scaling required. The case of $La_4Ni_3O_8$ is complicated by the La M_4 edge as well since, when measuring oriented crystals, the La M edge in FY shows a very strong polarization dependence due to the FY process and is not observed in the true XAS. This polarization dependence complicates direct scaling of the L_2 edge due to this strong polarization dependent background. Therefore, using the finding from the Pr case, we scale the data to match pre- and post-edge and the same points so that we could do a direct comparison. For these data, we chose the normalization points at 865 and 880 eV. For the data set shown in the text, which is from a longer run focused on just the L_2 edge, we chose the height of the c polarized $La_4Ni_3O_8$ to set the vertical scale. Following the standard procedure for normalizing the edge jump, the pre-edge level at 865 eV was subtracted to set that point to zero for both samples and polarizations. The vertical scale was defined by the height of the ab axis polarized $La_4Ni_3O_8$ scale, which was normalized to one. After this, we scale all data sets to match at 880 eV by multiplying the data sets by a scaling factor.

Quantitative evaluation of the orbital polarization. To obtain a quantitative estimate of the orbital character of the e_g bands, the sum rule for linear dichroism[9], which relates the total integrated intensity of the polarized spectra ($I_{E\|x}$ and $I_{E\|z}$) to the hole occupation $h_{3z^2-r^2}$ and $h_{x^2-y^2}$ in the e_g orbitals, is applied:

$$r = \frac{h_{3z^2-r^2}}{h_{x^2-y^2}} = \frac{3I_{E\|z}}{4I_{E\|x} - I_{E\|z}} \quad (1)$$

By this definition, r=0 corresponds to 100% $d_{x^2-y^2}$ orbital character in the unoccupied density of states, while r=1 occurs for equally populated orbitals.

Note that here we are only integrating the L_2 edge, but the sum rule for the L_2 edge can be derived by considering excitations from the $p_{1/2}$ core level to the e_g states. The integrated intensities in the dipole approximation are:

$$I_{E\|z,L_2} = \frac{c\, h_{3z^2-r^2}}{5} \quad (2)$$

$$I_{E\|x,L_2} = \frac{c\,(h_{3z^2-r^2} + 3h_{x^2-y^2})}{20} \quad (3)$$

where c is a constant involving the radial integrals. This leads to an orbital occupation ratio: $h_{3z^2-r^2}/h_{x^2-y^2} = 3I_{E||z}/(4I_{E||x} - I_{E||z})$, which is identical to that found for integration of the full $L_{2,3}$ edge shown in (1).

The edge jump, which represents excitations of electrons into the continuum, was set as a simple step function centered at the centroid of the ab axis polarization data. We have subtracted a step function background (see Supplemental Fig. 3*b*) to remove excitations into the continuum and integrated the spectra. We show the results for r in Supplemental Fig. 3*c* as a function of the integration range with the

starting point for integration defined by the onset of the XAS. For $YBa_2Cu_3O_7$, the integration yields $r(YBa_2Cu_3O_7) = 0.35$ and converges within a range 4 eV above the edge. Following the same procedure, with a 4 eV integration range, we find $r(La_4Ni_3O_{10}) = 1.06$ and $r(Pr_4Ni_3O_{10}) = 1.18$. The data for the $R_4Ni_3O_8$ do not converge as quickly, so we can examine r as a function of integration range. At 4 eV, $r(La_4Ni_3O_8)$ and $r(Pr_4Ni_3O_8)$ match that of YBCO with a value close to 0.35. The DFT results computed on the basis of the orbitally resolved density of states suggest that the integral will converge around 6 eV to a value ~0.45 (Supplemental Fig. 3*d*). Integration of the experimental spectra to 6 eV yields values of r in the range 0.4-0.5, in good agreement with the DFT result. For r=0.5, this means that the number of holes in $d_{x^2-y^2}$ is twice as big as $d_{3z^2-r^2}$, so we would obtain 67% of the holes in the $d_{x^2-y^2}$ orbital.

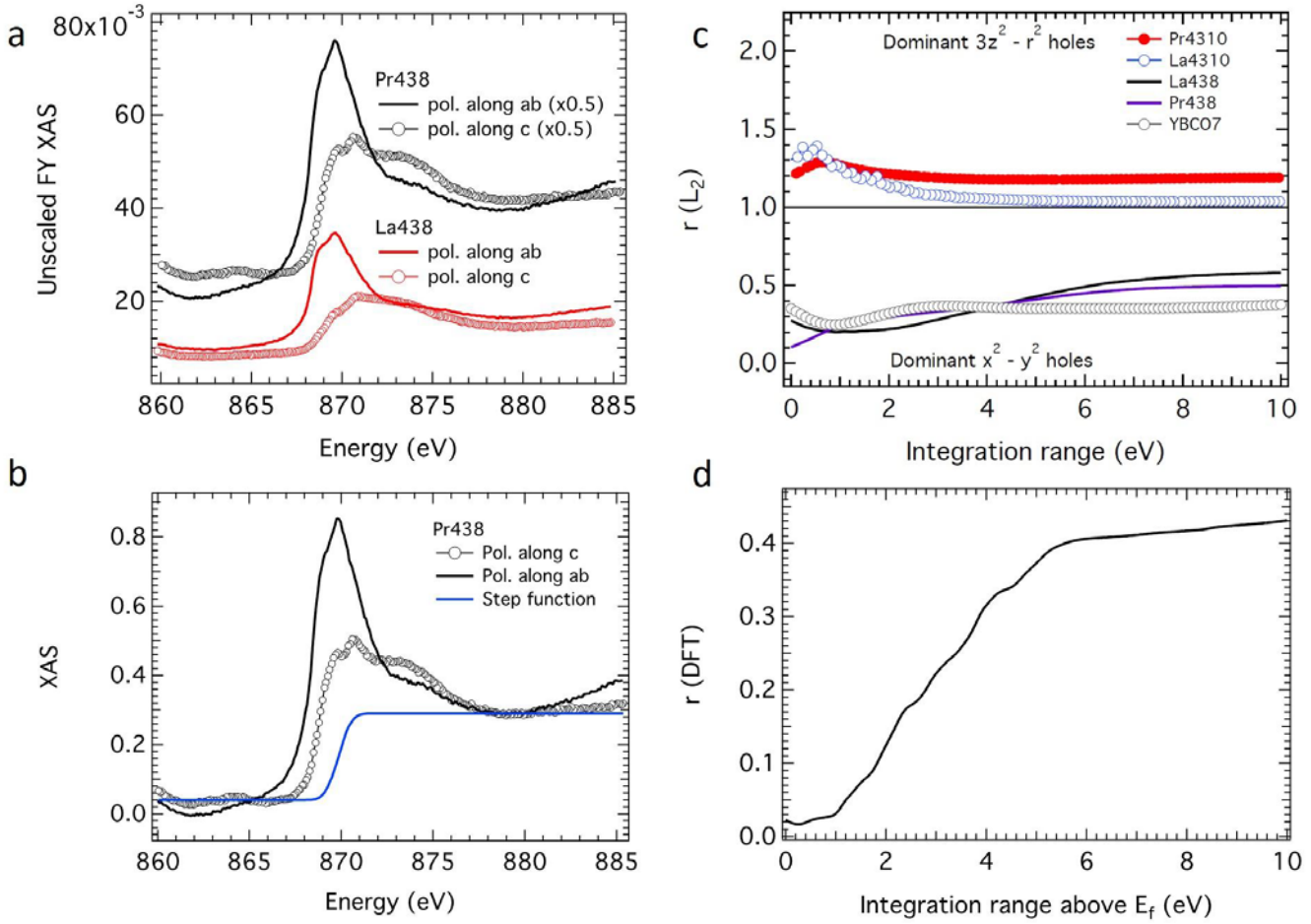

Supplemental Fig. 3. Quantitative evaluation of orbital polarization. (a) Raw, untreated full polarization dependent XAS scan across the L_2 edge. (b) Scaled data showing the step function used for background subtraction for $Pr_4Ni_3O_8$. (c) Integrated L_2 intensity as a function of the integration range. Pr4310: $Pr_4Ni_3O_{10}$; La4310: $La_4Ni_3O_{10}$; Pr438: $Pr_4Ni_3O_8$; La438: $La_4Ni_3O_8$; YBCO7: $YBa_2Cu_3O_7$ (Ref. 10). (d) Integration of the DFT-calculated orbitally resolved density of states for the LS state of $La_4Ni_3O_8$ as a function of the integration range.

S.4 Integrated Ni e_g DOS

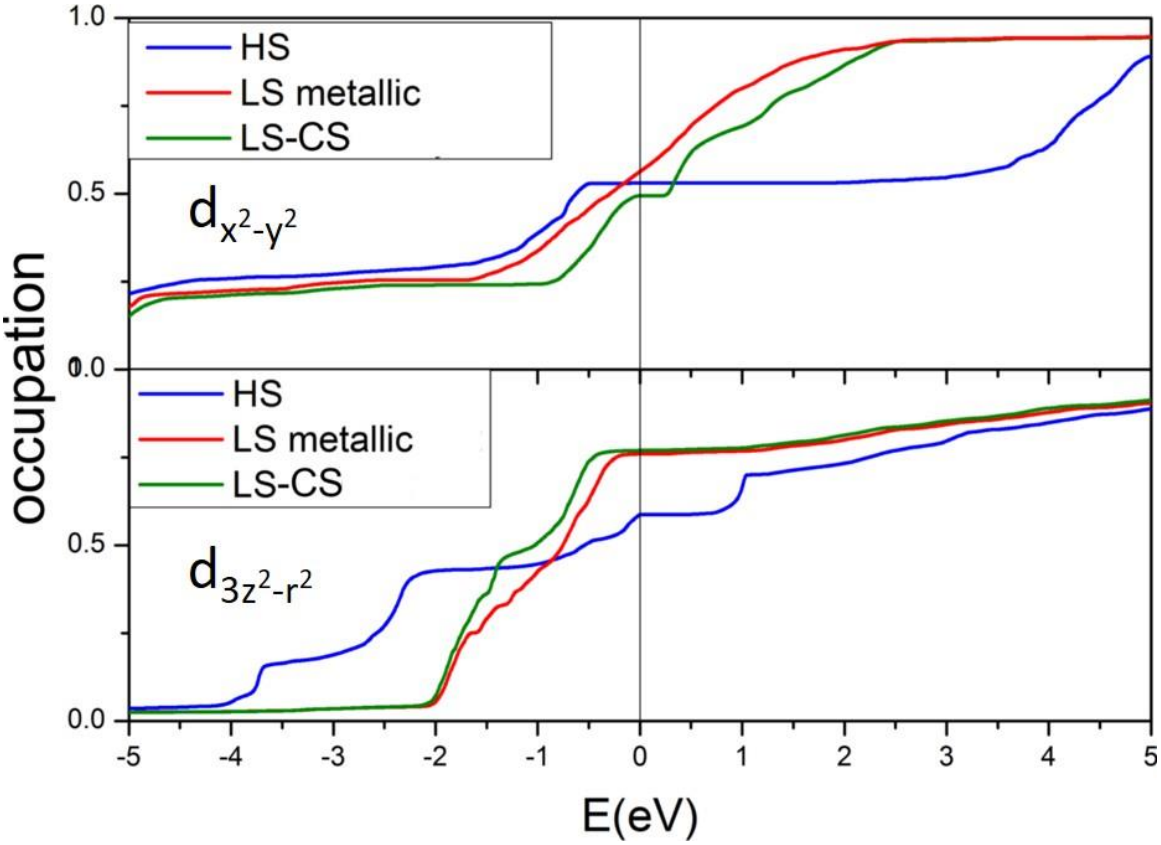

Supplemental Fig. 4. Integrated Ni e_g DOS for $La_4Ni_3O_8$ from DFT-calculations. Calculations are shown for the three different spin states shown in Fig. 2*b* of the main text. The Fermi energy is set at zero. XAS measurements in La438 show no change for the out of plane polarization and a very small change for in plane polarization across the transition. In terms of orbital occupations, this is consistent with the transition being from a LS-CS to a LS state: the occupation of the $d_{3z^2-r^2}$ orbitals does not differ and for the $d_{x^2-y^2}$ orbitals only a small change in occupation can be observed between these two states.

S.5 High Resolution Powder X-ray Diffraction (HR-PXRD).

To obtain the temperature dependence of unit cell parameters for $Pr_4Ni_3O_8$, HR-PXRD data were collected at beamline 11-BM at the Advanced Photon Source in the range $1° \leq 2\theta \leq 28°$ with a step size of 0.001° and wavelength λ=0.413367 Å. Samples were prepared by loading pulverized single crystals into a Φ0.8 mm Kapton capillary that was spun continuously at 5600 rpm during data collection. The obtained HR-PXRD data were analyzed using the GSAS[11] software with the graphical interface EXPGUI[12] using the single crystal structural model as a starting point. Refined parameters include background, intensity scale factor, 2θ zero offset, lattice parameters, atomic positions (except oxygen), isotropic atomic displacement parameters (U_{iso}, grouped by atomic species), and profile shape parameters. Shifted Chebyshev and pseudo-Voigt functions with anisotropic microstrain broadening terms (function #4)[13] were used for the background and peak profiles, respectively. The refinement of room temperature data ($1° \leq 2\theta \leq 50°$) converged to R_{wp}=12.06%, R_p=8.67% and χ^2=4.712, as shown in Supplemental Fig. 5.

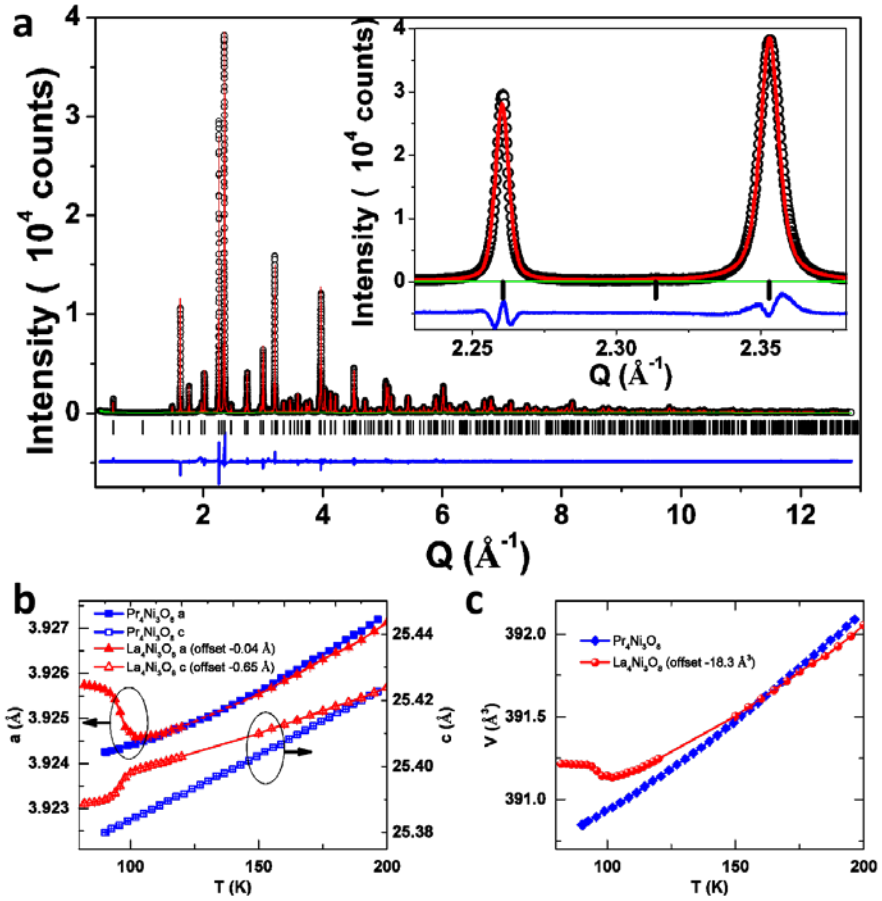

Supplemental Fig. 5. Rietveld refinement and temperature dependence of unit cell parameters of $Pr_4Ni_3O_8$ and $La_4Ni_3O_8$[14]. (a) High-resolution synchrotron x-ray diffraction pattern at room temperature. The black circles, red curve, green curve, black bars and blue curve correspond to the observed data, calculated intensity, background, Bragg peaks, and difference curve, respectively. The inset shows the quality of the fit in the Q range of 2.23-2.38 Å^{-1}. (b, c) Temperature dependence of unit cell parameters extracted from Rietveld refinements of high resolution powder x-ray diffraction data. Error bars reflecting the estimated standard deviation from the refinement are smaller than symbols.

S.6 High resolution single crystal synchrotron x-ray diffraction

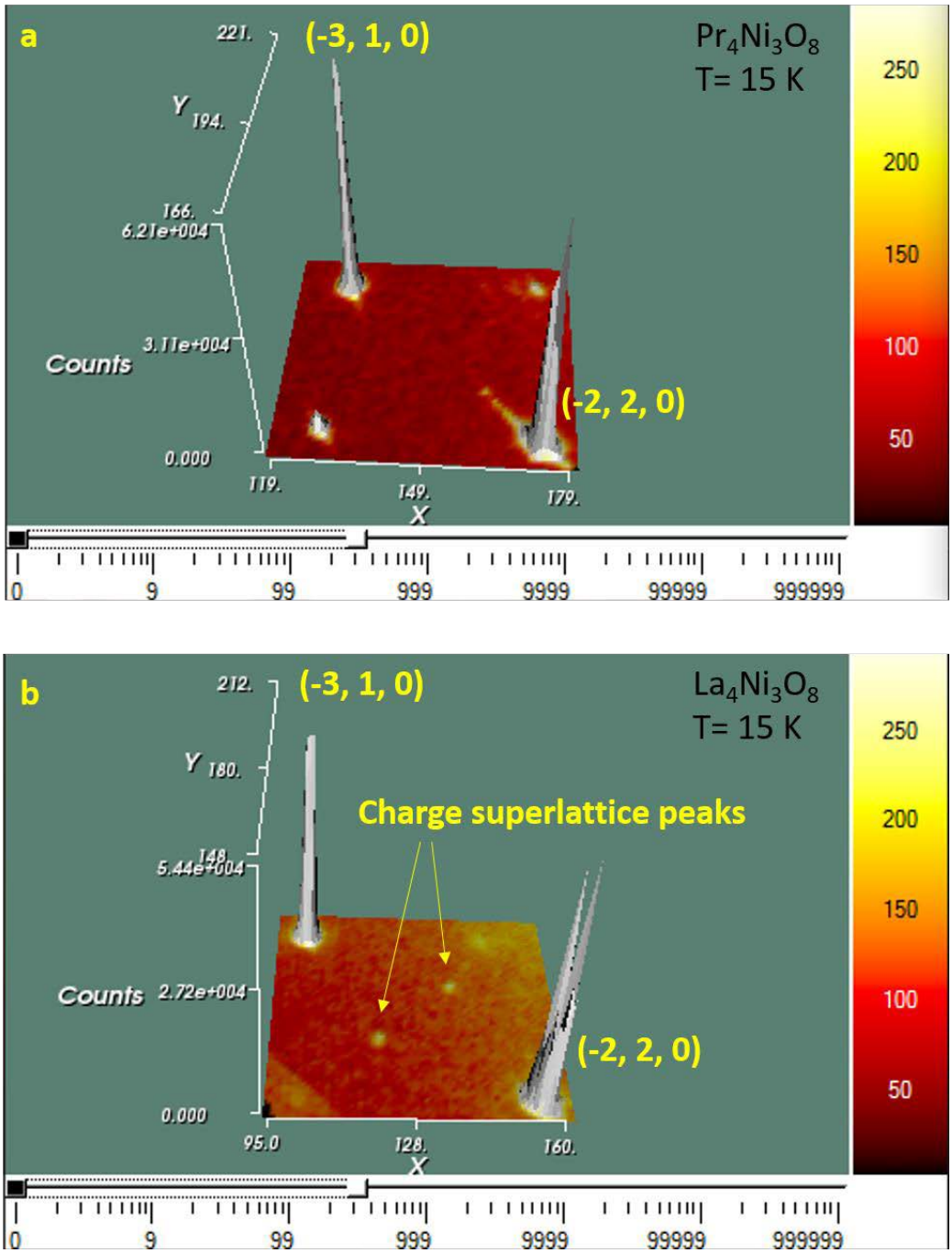

Supplemental Fig. 6. High resolution single crystal x-ray diffraction of $Pr_4Ni_3O_8$ and $La_4Ni_3O_8$ at 15 K. The intensity of superlattice peaks in $La_4Ni_3O_8$ is about five orders weaker than strongest Bragg peaks, and was successfully observed as shown in (*b*). In contrast, no superlattice peaks were observed in (*a*) for $Pr_4Ni_3O_8$.

S.7 DFT calculations on $Pr_4Ni_3O_8$.

As mentioned in the main text, a full study on the stability of the different spin states for $Pr_4Ni_3O_8$ has been performed within two different LDA+*U* schemes: around mean field (AMF) and fully localized limit (FLL)[15-17]. Supplemental Table 3 shows the Ni magnetic moments for these two different DFT+*U* methods ($1.36 \leq U_{Ni} \leq 8.16$ eV, $J_{Ni}=0.68$ eV; $U_{Pr}=9.5$ eV, $J_{Pr}=1.0$ eV) as well as the insulating/metallic character of each of the derived states. The low-spin (LS) state has a ferromagnetic in-plane coupling, while the high spin state (HS) has an antiferromagnetic one, in agreement with previous work on the La compound[7,18,19]. Supplemental Fig. 7 shows the energy difference between HS and LS states for intermediate *U* values from 2.72 to 6.8 eV for both AMF and FLL. Within the AMF LDA+*U* flavor, the LS state in $Pr_4Ni_3O_8$ is favored independent of *U*. However, the FLL flavor only favors the LS state at low values of *U,* whereas at high values of *U* (sufficient to open a gap in the high-spin solution, and hence inconsistent with experimental evidence), the high-spin solution is favored. These trends are consistent with earlier results on the La compound, except there, for the AMF scheme the HS state becomes stable once *U* exceeds 6.5 eV, and for the FLL scheme, the HS is stable regardless of the *U* value.[19] Hence, the smaller unit cell volume of $Pr_4Ni_3O_8$ vs $La_4Ni_3O_8$ tends to stabilize a LS state.

These results can be understood from the fact that the AMF scheme is known to favor the stabilization of low spin configurations, whereas FLL tends to favor high spin configurations[20]. This is a direct consequence of the double counting term in the AMF scheme giving magnetic states a larger energy penalty than does the FLL one, as clearly reflected in the values of the magnetic moments in Supplemental Table 3.

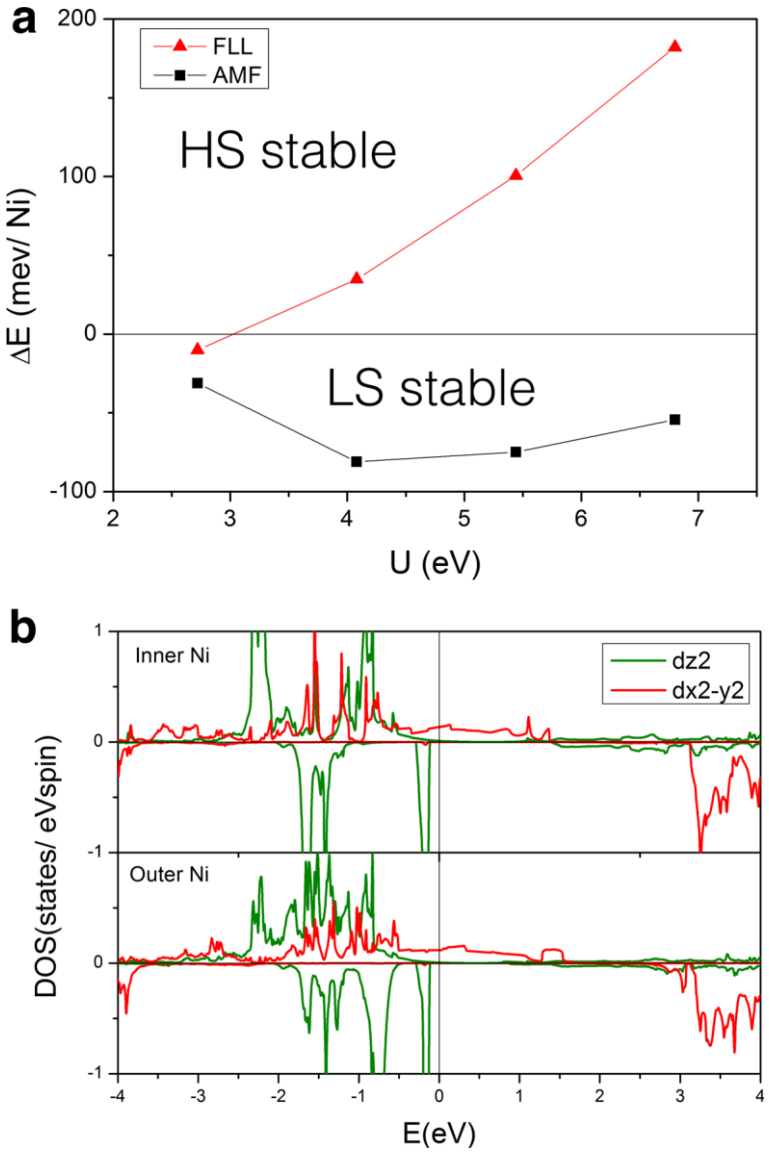

Supplemental Fig. 7. DFT calculations for $Pr_4Ni_3O_8$. (a) Energetics of the spin states comparing the low-spin (LS) and high-spin (HS) solutions using two different LDA+*U* flavors. The stability of the LS phase is clear for the "around mean field" flavor consistent with previous calculations[19,21] for $La_4Ni_3O_8$. For $Pr_4Ni_3O_8$ a LS-charge stripe state could not be obtained. (b) Calculated orbital resolved density of states of Ni atoms in $Pr_4Ni_3O_8$ for U=5.44 eV and J=0.68 eV for Ni. Note the upper part of each panel is for spin up, and the lower part for spin down.

Supplemental Table 3. Ni atomic magnetic moments (MM) (in μ_B) of Pr438 for the different DFT+U methods used in this work, for different U values for both HS and LS states (J_{Ni}=0.68 eV, U_{Pr}=9.5 eV, J_{Pr}=1.0 eV). There are two Ni atoms in each inner plane (Ni1 and Ni2) and two Ni atoms in each outer plane (Ni3 and Ni4). The insulating/metallic character of each state is indicated. The calculated Pr magnetic moment is always ~ 2 μ_B independent of the model. Note spin-orbit coupling was not included.

High spin state

U (eV)	DFT+U Flavor	MM Ni1	MM Ni2	MM Ni3	MM Ni4	Insulating (I) /metallic (M)
1.36	FLL	0.50	-0.54	0.37	-0.40	M
2.72	FLL	1.14	-1.14	1.01	-1.01	M
4.08	FLL	1.26	-1.26	1.14	-1.15	I
5.44	FLL	1.30	-1.30	1.20	-1.21	I
6.8	FLL	1.43	-1.43	1.30	-1.30	I
8.16	FLL	1.50	-1.50	1.37	-1.37	I
1.36	AMF	0.48	-0.40	0.36	-0.29	M
2.72	AMF	0.59	-0.57	0.35	-0.52	M
4.08	AMF	1.18	-1.16	1.03	-0.99	M
5.44	AMF	1.26	-1.25	1.11	-1.07	I
6.8	AMF	1.33	-1.33	1.15	-1.11	I
8.16	AMF	1.40	-1.40	1.22	-1.18	I

Low spin state

U (eV)	DFT+U Flavor	MM Ni1	MM Ni2	MM Ni3	MM Ni4	Insulating (I) /metallic (M)
1.36	FLL	0.58	0.58	0.58	0.58	M
2.72	FLL	0.69	0.69	0.66	0.66	M
4.08	FLL	0.72	0.72	0.70	0.70	M
5.44	FLL	0.86	0.86	0.86	0.86	M
6.8	FLL	0.76	0.76	0.73	0.73	M
8.16	FLL	0.79	0.79	0.79	0.79	M
1.36	AMF	0.57	0.57	0.57	0.57	M
2.72	AMF	0.67	0.67	0.67	0.67	M
4.08	AMF	0.68	0.68	0.68	0.68	M
5.44	AMF	0.68	0.68	0.65	0.65	M
6.8	AMF	0.66	0.66	0.64	0.64	M
8.16	AMF	0.22	0.22	0.33	0.33	M

S.8 Pr *M* edge XAS

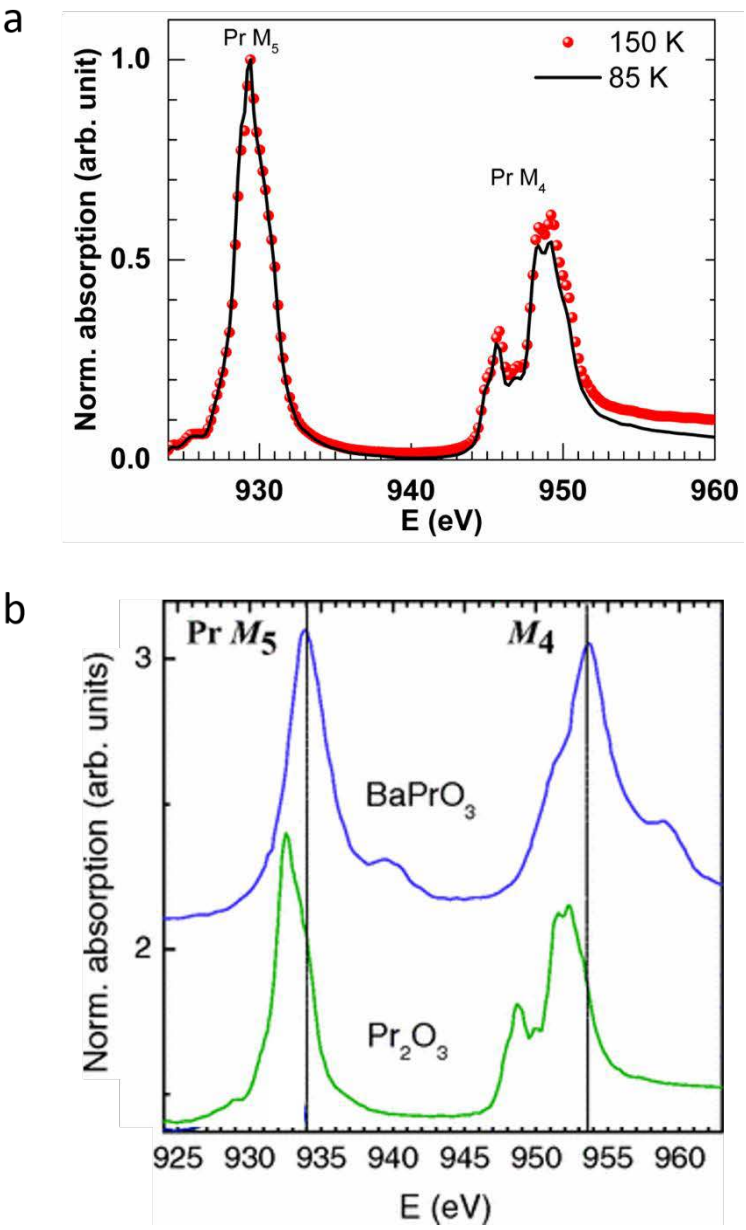

Supplemental Fig. 8. Pr *M* edge XAS. (a) Pr M edge XAS data of $Pr_4Ni_3O_8$ collected at 85 and 150 K. (b) XAS data for Pr^{3+} and Pr^{4+} reference materials Pr_2O_3 and $BaPrO_3$ (Ref. 22). The spectrum shows no compelling evidence for Pr^{4+} in $Pr_4Ni_3O_8$.

References

1 Bruker AXS, Inc. APEX2 (Bruker AXS, Inc. Madison, WI, USA) (2014).

2 Bruker AXS, Inc. Computer code SHELXTL (Bruker AXS, Inc. Madison, WI, USA) (2014).

3 Freeland, J. W., van Veenendaal, M. & Chakhalian, J. Evolution of electronic structure across the rare-earth $RNiO_3$ series. *J. Electron. Spectrosc. Relat. Phenom.* **208**, 56-62 (2016).

4 Abbate, M. *et al.* Electronic structure and metal-insulator transition in $LaNiO_{3-x}$. *Phys. Rev. B* **65**, 155101 (2002).

5 Petrie, J. R. *et al.* Strain Control of Oxygen Vacancies in Epitaxial Strontium Cobaltite Films. *Adv. Funct. Mater.* **26**, 1564-1570 (2016).

6 Saitoh, T. *et al.* Electronic structure and magnetic states in $La_{1-x}Sr_xCoO_3$ studied by photoemission and x-ray-absorption spectroscopy. *Phys. Rev. B* **56**, 1290-1295 (1997).

7 Poltavets, V. V. *et al.* Bulk magnetic order in a two-dimensional Ni^{1+}/Ni^{2+} (d^9/d^8) nickelate, isoelectronic with superconducting cuprates. *Phys. Rev. Lett.* **104**, 206403 (2010).

8 Morrow, R. *et al.* Magnetism in Ca_2CoOsO_6 and Ca_2NiOsO_6: Unraveling the Mystery of Superexchange Interactions between 3*d* and 5*d* Ions. *Chem. Mater.* **28**, 3666-3675 (2016).

9 van der Laan, G. Sum Rules and Fundamental Spectra of Magnetic X-Ray Dichroism in Crystal Field Symmetry. *J. Phys. Soc. Jpn.* **63**, 2393-2400 (1994).

10 Hawthorn, D. G. *et al.* Resonant elastic soft x-ray scattering in oxygen-ordered $YBa_2Cu_3O_{6+\delta}$. *Phys. Rev. B* **84**, 075125 (2011).

11 Larson, A. C. & Dreele, R. B. V. General Structure Analysis System (GSAS) (Los Alamos National Laboratory, Los Alamos, NM), Tech Rep LAUR 86-748 (2004).

12 Toby, B. H. EXPGUI, a graphical user interface for GSAS. *J. Appl. Crystallogr.* **34**, 210-213 (2001).

13 Stephens, P. W. Phenomenological model of anisotropic peak broadening in powder diffraction. *J. Appl. Crystallogr.* **32**, 281-289 (1999).

14 Zhang, J. *et al.* Stacked charge stripes in the quasi-2D trilayer nickelate $La_4Ni_3O_8$. *Proc. Natl. Acad. Sci. U.S.A.* **113**, 8945-8950 (2016).

15 Liechtenstein, A. I., Anisimov, V. I. & Zaanen, J. Density-functional theory and strong interactions: orbital ordering in Mott-Hubbard insulators. *Phys. Rev. B* **52**, R5467-R5470 (1995).

16 Petukhov, A. G., Mazin, I. I., Chioncel, L. & Lichtenstein, A. I. Correlated metals and the LDA+*U* method. *Phys. Rev. B* **67**, 153106 (2003).

17 Czyżyk, M. T. & Sawatzky, G. A. Local-density functional and on-site correlations: the electronic structure of La_2CuO_4 and $LaCuO_3$. *Phys. Rev. B* **49**, 14211-14228 (1994).

18 Pardo, V. & Pickett, W. E. Quantum confinement induced molecular correlated insulating state in $La_4Ni_3O_8$ *Phys. Rev. Lett.* **105**, 266402 (2010).

19 Pardo, V. & Pickett, W. E. Pressure-induced metal-insulator and spin-state transition in low-valence layered nickelates. *Phys. Rev. B* **85**, 045111 (2012).

20 Ylvisaker, E. R., Pickett, W. E. & Koepernik, K. Anisotropy and magnetism in the LSDA+*U* method. *Phys. Rev. B* **79**, 035103 (2009).

21 Botana, A. S., Pardo, V., Pickett, W. E. & Norman, M. R. Charge ordering in Ni^{1+}/Ni^{2+} nickelates: $La_4Ni_3O_8$ and $La_3Ni_2O_6$. *Phys. Rev. B* **94**, 081105(R) (2016).

22 Herrero-Martín, J. *et al.* Valence change of praseodymium in $Pr_{0.5}Ca_{0.5}CoO_3$ investigated by x-ray absorption spectroscopy. *Phys. Rev. B* **84**, 115131 (2011).